FCC-hh conceptual designs and windability of the Main Quadrupoles

C. Genot, C. Lorin, G. Minier, E. Pepinter, Y. Rabti, E. Rochepault, T. Salmi, D. Schoerling, D. Tommasini

Abstract— **In the framework of a design study for a post-LHC 100 TeV circular hadron collider, namely FCC-hh, high gradient Nb₃Sn lattice quadrupoles were investigated, following closely the specifications from the optic layout of that machine. After several iterations, a baseline design of the Main Quadrupole (MQ) was selected and, then, included in the FCC-hh Conceptual Design Report. The paper deals with the preliminary results of the 3D electromagnetic and mechanical conceptual design. The 3D design of Nb₃Sn coil ends is known to be a critical phase, especially for small apertures. To tackle the potential issues, 3D electromagnetic design was first carried out, taking into account the field quality constraints, the field margins in critical areas, and the windability of the coil ends. Then, winding trials with actual cables were performed, to help selecting designs and identifying critical geometrical parameters.**

Index Terms—**Nb₃Sn coil, collar structure, winding trials, MQ**

I. INTRODUCTION

The European Strategy for Particle Physics update in 2013 stated "To stay at the forefront of particle physics, Europe needs to be in a position to propose an ambitious post-LHC accelerator project at CERN […]. CERN should undertake design studies for accelerator projects in a global context […]. These design studies should be coupled to a vigorous accelerator R&D programme, including high-field magnets […], in collaboration with national institutes, laboratories and universities worldwide"[1]. This study on the FCC-hh Main Quadrupole is a spin-off of this recommendation. Indeed, CERN and CEA set-up a collaboration agreement to investigate, among other, high gradient quadrupoles for the FCC-hh lattice. Preliminary design studies have already been carried out [2][3], and focused particularly on conductor parametric studies, the 2D magnet cross-section, protection investigation, the random positioning of the conductor, and the magnetization effects. A short summary of these study can also be found in the FCC-hh Conceptual Design Report [4]. Since then, the investigation was pushed further toward a 3D electromagnetic and mechanical designs coupled to winding trials. The study was conducted in parallel with the H2020 EuroCirCol (ECC) project [5]. Indeed, in terms of magnet performance, this study went along with the investigation of the optics layout of the FCC-hh machine requiring a 360 T/m quadrupole magnet of 7.2 m in length with a 50 mm aperture [6] – WP2 of the ECC project. On the other hand, conductor

performances and magnet material properties were in line with the ones of the FCC-hh 16 T dipole magnet designed in the frame of the WP5 of the ECC project. This ECC project was itself included in the CERN 16 T magnet technology program [7][8]. For clarity's sake, some of the data already published in [3] may be recalled to make the paper self-consistent, particularly the conductor features and the 2D magnet cross-section. However, for example, the protection investigation, the random positioning of the conductor, the magnetization effect will not be recalled. Therefore, after a short contextualization, the magnet strand and cable are briefly described in a section mainly dedicated to the 3D electromagnetic design of the FCC-hh MQ. In a second section, winding trials, performed with cables available at the time of the study, are reported. A preliminary 3D mechanical analysis is reported elsewhere [9].

A. Conductor features

FCC-hh high field magnets rely on conductors performing at $J_c = 1500$ A/mm² @ 4.2 K and 16 T corresponding to $J_c = 2300$ A/mm² @ 1.9 K and 16 T. Obviously, the critical current is of utmost importance, nevertheless the effective filament diameters or the strand unit lengths are also very challenging features tackled by the CERN FCC conductor development program [10]. A degradation of ~3% is expected to occur while cabling. The critical current J_c of the Nb₃Sn conductor can be parameterized as follow:

$$\begin{cases} J_c = \dfrac{C(t)}{B} b^{0.5}(1-b)^2 \\ B_{c2}(T) = B_{c20}(1-t^{1.52}) \\ C(t) = C_0(1-t^{1.52})^\alpha(1-t^2)^\alpha \end{cases}$$

where $t = T/T_{c0}$ and $b = B/B_{c2}(t)$ and B is the magnetic flux density on the conductors. $T_{c0} = 16$ K, $B_{c20} = 29.38$ T, $\alpha = 0.96$, $C_0 = 275880$ AT/mm² are extrapolated fitting parameters. The dimensions of the FCC-hh MQ cable are reported in Table I.

Dimensions of both the MQXF and LHC MQ cables are provided for comparison as they were used to carry out some windings trials (see section III).

TABLE I
CABLE CHARACTERISTICS OF FCC MQ, MQXF AND LHC MQ

MQ parameters	Units	FCC	MQXF [11]	LHC
Material	-	Nb$_3$Sn	Nb$_3$Sn	Nb-Ti
Strand diameter	mm	0.85	0.85	0.825
Cu/nonCu	-	1.65	1.2	1.95
Number of strands	-	35	40	36
Bare width/reacted	mm	15.956/16.12	18.15/18.363	15.1
Bare thickness/reacted	mm	1.493/1.538	1.525/1.594	1.48
Bare thin edge/reacted	mm	1438/1.481	1.462/1.530	1.362
Bare thick edge/reacted	mm	1.549/1.596	1.588/1.657	1.598
Keystone angle	°	0.4	0.4	0.9
Transposition pitch	mm	96	109	100
Insulation thickness	µm	150	145	142.5
Reaction width expansion	%	~1	~1	N/A
Reaction thickness expansion	%	~3	~4	N/A

B. 2D electromagnetic design reminder

The 2D design was already shown in [3] and its main features are reported in Table II. It is worth noticing that the 2D design, reported in Fig. 1, was slightly modified after the 3D electromagnetic study to avoid any easy-way bending of the cable over the layer jump. To do so, the tilt angle of the upper block of the outer layer was changed from 24.5° to 23°. This did not impact any of the 2D analysis (electromagnetic or mechanical).

TABLE II
MAIN MAGNET FATURES

Parameters	Units	FCC MQ (v12)
Nominal gradient	T/m	367
Aperture	mm	50
Nominal current	A	22500
Peak field at nominal	T	10.52
Load-line margin	%	20.1
Temperature margin	K	4.6
Inductance (2 apertures)	mH/m	2.04
Stored energy (2 apertures)	kJ/m	520
Azimuthal force per ½ coil	MN/m	1.74
Radial force per ½ coil	MN/m	0.4
Axial force per aperture	kN	260
Midplane shim	µm	325
Interlayer insulation	mm	0.5
Number of turns per layer	-	8 + 10
Area of conductor per magnet	cm²	57.2
Estimated weight of conductor*	tonnes	270

*Weight estimated for the 744 MQs of the FCC-hh with a conductor density

C. 3D electromagnetic design

The 3D electromagnetic design was performed in two iterations. For each iteration, i) a model was built with the ROXIE software to define the coil end geometry by minimizing both the strain energy of the cable [12] and the integrated harmonics along the magnet axis; ii) then, the coil geometry was transferred to OPERA in order to investigate the peak field in the coil ends and the layer jump by mainly playing on the yoke length; iii) finally, the raw end spacer geometry was transferred

from ROXIE to CATIA software to implement some mechanical features to the end spacers and draw the tooling needed to perform the winding trials. All the end spacer sets produced in the frame of that study were 3D printed by Fused Deposition Modeling with ABSplus plastic. As described in [12], the ROXIE software allows for defining the shape of the cable over the coil head by optimizing i) the ellipticity and ii) the order of the hyper-ellipse baseline on the mandrel - the baseline represents the cable lower edge outline on the mandel – iii) the angle β between the innermost cable turn and the mandrel at the curvature apex (Fig. 2) and four cable torsion along the cable between the apex and the turn end.
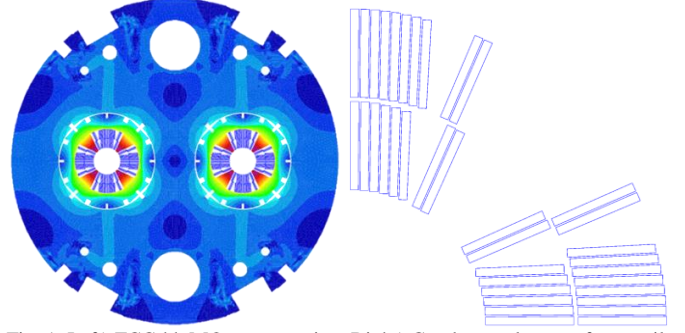

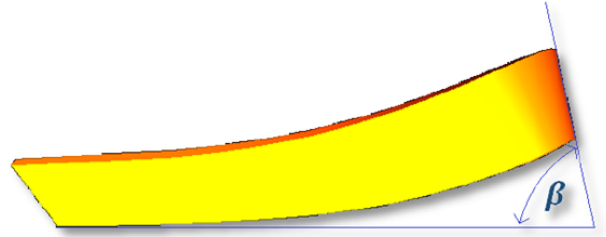Fig. 1. Left) FCC-hh MQ cross-section. Right) Conductors layout of one coil.

Fig. 2. Cable turn side view with the angle β at the apex of the turn.

In Fig. 3 is reported the 3D design of the OPERA model. It is worth noticing that the model should not be considered symmetrical with respect to the vertical or horizontal axis of the magnet due to the layer jump and coil lead end. Yoke or collar should be fully modeled. Indeed, the two apertures are identical and do not mirror each other, that is to say that an aperture is obtain by a translational movement on the other aperture and not by a symmetry with respect to a plane. Therefore, two OPERA models – one with vertical and horizontal symmetries and another one with the full model - allowed verifying that taking into account the symmetries does not impact the results – the model with symmetries was used to shorten the computational time since many simulations was run during the electromagnetic study. In Fig. 4 the normalized OPERA harmonics $b_n(z) = B_n(z)/B_2(z=0) \times 10^4$ over the magnet length are compared to the ROXIE results. There is only a slight b_6 discrepancy at the upper part of the layer jump that has not been understood so far.
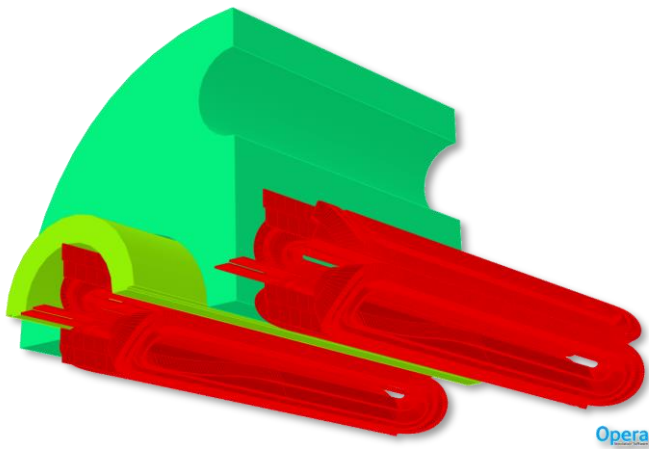
Fig. 3. 3D OPERA model of the FCC-hh main quadrupoles. The coils of the two apertures are fully represented with the lead end and the layer jump on the left side. Over the straight part the collars have a nose that is removed over the coil heads. The main hole of the yoke, used for heat exchange, is modeled.
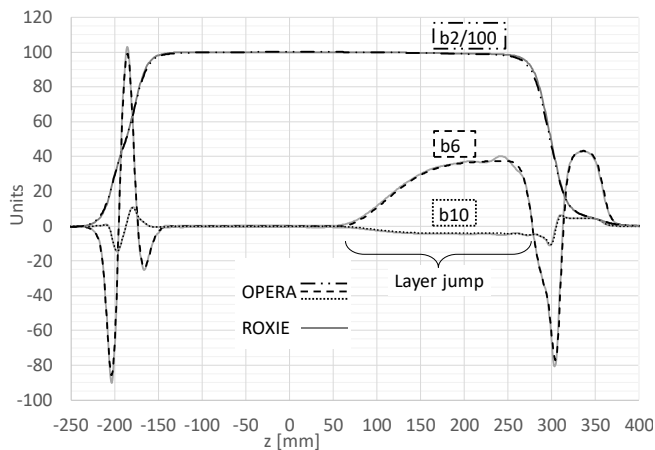

Fig. 4. Comparison of the first allowed normalized multipole b_2, b_6, and b_{10} between OPERA model and ROXIE model. On the left side is the return end of the coil. In the straight part, b_6 and b_{10} are lower than the unit. Over the layer jump, b_6 increases to reach ~40 units. On the right side, the 5-cm extra connection cables of the lead end generate a b_6 of slightly more than 40 units

The integrated gradient required by the optics is 2592 T [6]. Based on our nominal gradient of 367 T/m, the magnetic length becomes 7.06 m. The short model being only 425 mm long, the magnet length – actually its straight part - is virtually increased in the calculation of the integrated harmonics. The final design led to an integrated b_6 of 0.76 units and an integrated b_{10} of -0.44 units, the data are reported in Table III.

TABLE III
3D INTEGRATED HARMONICS, ROXIE

Magnet section	b_6 [units]	b_{10} [units]	Magnetic length [mm]
Return end	-2.14	-0.76	77.4
Lead end	21.37	-2.83	282.6
Straight section/2D	-0.08	-0.33	6700.0
Full length	0.76	-0.44	7060.0

The peak field was investigated in the magnet along the path of the polar cable of the inner coil as shown in Fig. 5. The peak

field in the straight part was observed to be 0.8% lower in OPERA than in ROXIE (ROXIE: 10.52 T; OPERA: 10.44 T). This discrepancy has been observed in previous simulations and is likely due to the different way of modelling the current distribution in ROXIE (current lines) and in OPERA (current density). In our design, in order to reduce the peak field (located in the return end, see Fig. 5), and bring it closer to the field of the straight section, the iron yoke was shortened by 50 mm and a 3 mm end spacer was added in-between the first two turns of the coil return end . The field in the layer jump is only 0.06 T higher than in the straight section (Fig. 5). The impact of this additional end spacer on the integrated b_6 is negligible, less than 0.01 unit over the full magnet length, as shown in Fig. 6.
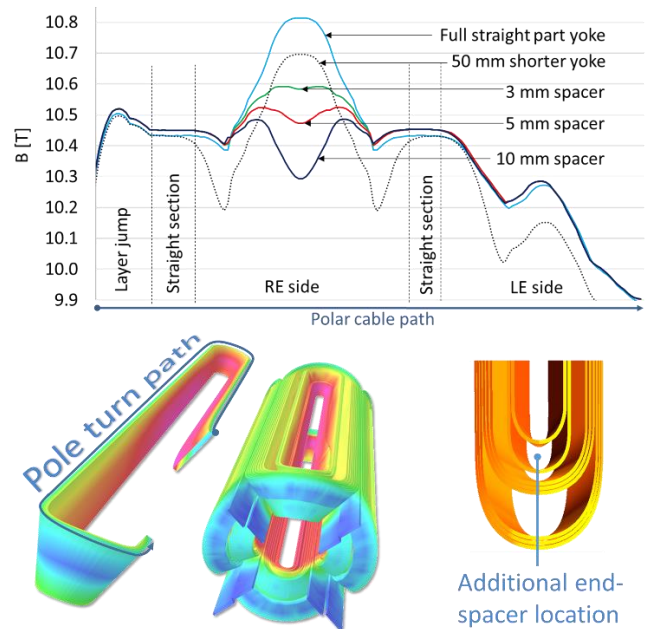

Fig. 5. Lower part left: Location of the pole turn path where the peak field is evaluated. The peak field is the maximal magnetic field values over the width of the cable. Lower part right: Location of the additional end-spacer over the coil return end. Upper part: The peak field is plotted along the innermost polar cable for two yoke sizes and three different end spacer thicknesses (3 mm, 5 mm and 10 mm).
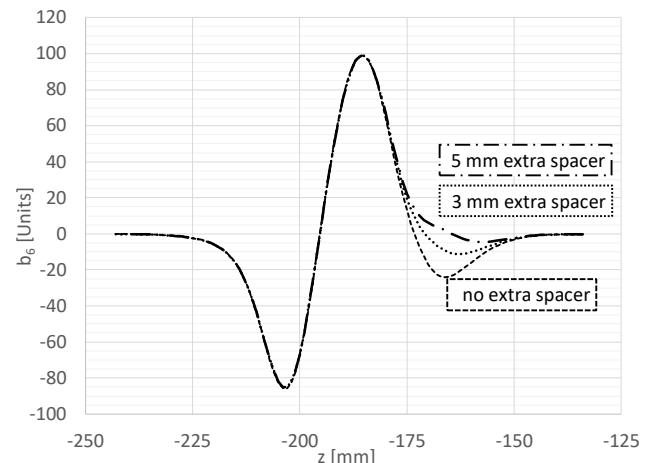

Fig. 6. Impact on b_6 of the extra end spacer, located between the first two turns of the return end, with respect to the initial design with no extra spacer

As described in the next section, a second magnet design iteration was realized to improve the coil windability in addition of magnetic considerations.

II. WINDING TRIALS

A. Background

Several winding trials were carried out using an initial design of the end spacers, and were used to re-optimize the design based on experimental experience. Only the tests on the final design will be reported here. Actually these preliminary tests allow us to tune the angle β and therefore have a better curvature to reduce the gap between the mandrel and the cable. A ROXIE-CATIA routine was used to create the end-spacers. They were printed with FDM technology (Fused Deposition Modeling). The objective was, in one hand to check that the superconducting cable properly laid on the end-spacers and on the mandrel, and on the other hand to observe the behavior of the cable at the coil ends like a strand jumping out of the cable due to a too high cable strain energy due to winding: the so-called pop-up strand, or a curvature of the cable cross-section into a C-shape referred to as dishing. Thus, the use of end-spacers made of ABSpluS-P430 (thermoplastic) was sufficient for the winding trials. A full set of tooling offering the possibility to guide and lock the cable while winding was at disposal (Fig. 7). The winding trials were carried out with two different types of cable, the LHC MQ Nb-Ti cable (for preliminary tests) and the MQXF Nb$_3$Sn cable. The features of both of them are reported in TABLE I next to the FCC MQ ones. The LHC MQ cable was used in order to have a cable closer in terms of dimension to the FCC-hh MQ one bearing in mind that Nb-Ti cables are stiffer than Nb$_3$Sn cables. The MQXF cable was dimensionally the closest one available in Nb$_3$Sn. Many trials were carried out without the polyimide or glass fiber insulations for visual inspection.
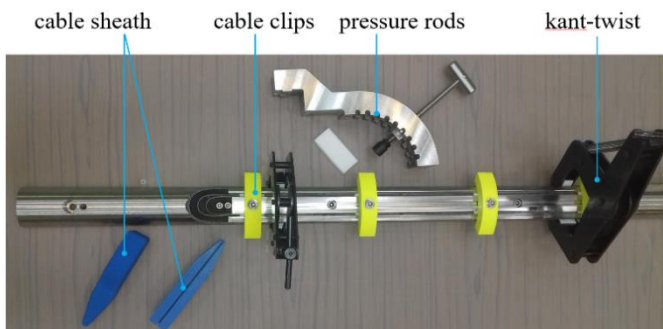

Fig. 7. Tooling developed for the various winding trials allowing to lock or unlock the cable at will while winding. Cable clips help to support the cable radially and kant-twists in the azimuthal direction. The pressure rods allow to push radially onto the cable or end spacers. The cable sheath allows to minimize strand pop-up during the winding.

B. Preliminary winding trials with LHC MQ cable

Only the first turns of the winding where the stress is high were done. The winding tensions were arbitrarily set at 20 kg for the straight section and 10 kg over the coil ends. No strand pops out of the cable while going around the pole. Nevertheless,

due to its stiffness a protrusion of 2 mm between the mandrel and the cable is observed on both sides of the turn (Fig. 8Fig. 9) [13][14].

In any case, these first tests were only preliminary to gain in experience and could not be fully conclusive due to the stiffness of the Nb-Ti cable. Therefore a second campaign more structured was carried out with a Nb$_3$Sn cable.
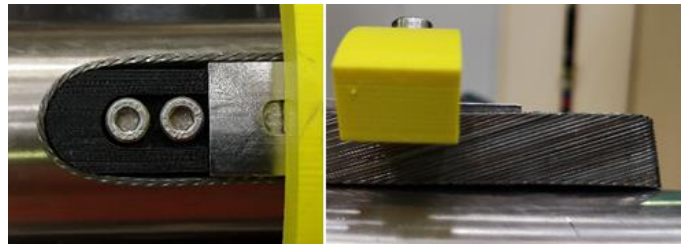

Fig. 8. Left: Top view of the first turn with the LHC MQ cable. The cable lays on the pole but does not accommodate the mandrel curvature. A gap of 2 mm between the mandrel and the cable cannot be recovered
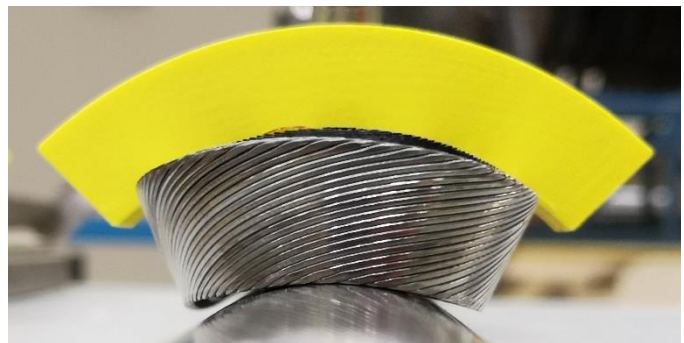

Fig. 9. View along the axis of the mandrel showing the gap between the mandrel and the LHC MQ cable after several turns.

C. Winding trials with MQXF cable, first turn RE

With the MQXF cable, the winding tension was changed (10 kg, 20 kg, 30 kg) and several trials with the cable locked or unlocked radially and azimuthally before the turn starts were performed. The best configuration found was: (i) using a tension of 20 kg; (ii) first unlocking the cable while making the turn (just constrained with the cable sheath), then (iii) maintaining the cable azimuthally in the straight part with a kant-twist and a long bar and (iv) finally pushing back radially the cable in contact to the mandrel via the pressure rods. Nonetheless, a strand always in the same area of the turn was popping out (Fig. 10), an innermost strand in contact with the mandrel close to the apex. The problem is seen half of the twist pitch further on the cable edge when the strand *emerges*.
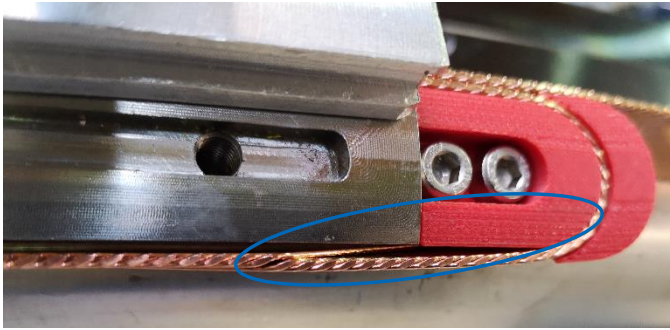
Fig. 10. Recurring strand popping out of the cable while winding the first turn regardless of the winding tension or winding procedure.

During those trials it was observed that the protrusion was propagating along the cable every transposition pitch. Indeed, pushing with the yellow cable clips onto the cable edge after the turn displaces the protrusion a twist pitch further (Fig. 11).
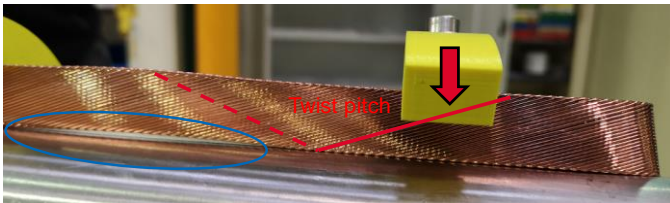

Fig. 11. Propagation of the protrusion along the straight section while pushing onto the cable with the yellow clips.

D. Winding trials with MQXF cable, partial winding

A partial winding, Fig. 12, was attempted in order to experiment on the difficult turns after the copper wedge where the cable is still almost horizontal, due to the low keystone angle, but high in the aperture (Fig. 1). A tension of 20 kg was set and the best procedure, as previously described, was used.
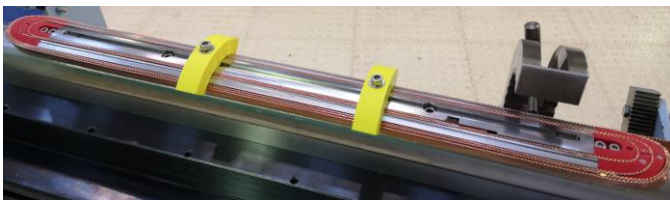

Fig. 12. Partial winding including 5 out of 8 turns of the inner layer.

This last trial indicates that the curvature of the cable turns after the copper wedges was probably made with a too high hardway bend leading to cable openings in the lead end of the coil (Fig. 13) [14]. Nevertheless, to achieve this partial winding, end-spacers, made of ABS, were used, and were slightly deformed during winding (Fig. 14). This deformation changes the position of the cable and thus may impact the behavior of the cable and partially question the previous cable openings.
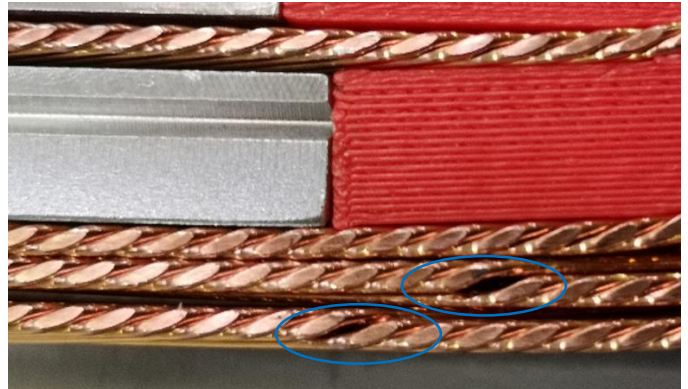

Fig. 13. Cable opening during the winding of the lead end potentially due to the hardway bend of the cable [14].

Finally, this winding campaign was instructive about the risk of using a cable of this size on a 50 mm diameter mandrel in a quadrupole configuration. Even though slightly oversized compare to the FCC-hh MQ cable, the winding failure with the MQXF cable shall be seriously considered. 0.85 mm strands should be avoided for further designs of the inner layer of the FCC-hh Main Quadrupole.
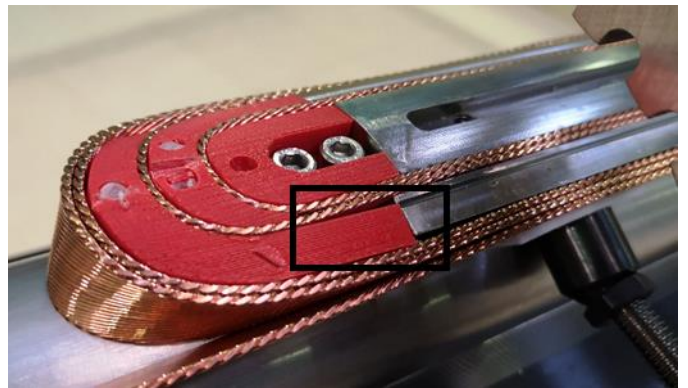

Fig. 14. Lead end of the coil with the end spacer deformation in the black box.
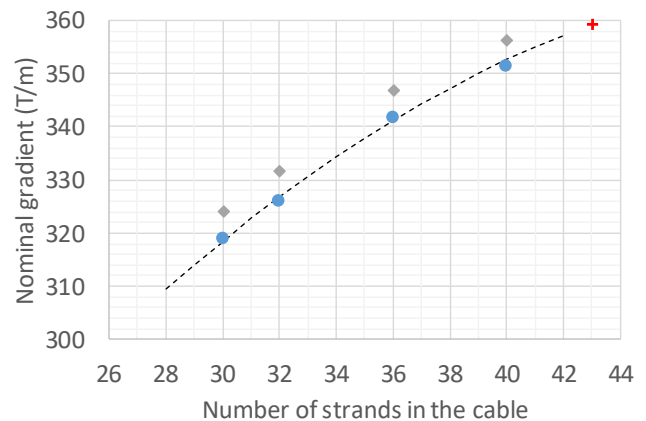

Fig. 15. Nominal gradient of the quadrupole versus the number of strands in the cable. The blue dots represent the four 2D design data with a 20% margin which are fitted by the dash curve. The grey squares are additional data with a 16% loadline margin. The red cross is a design with 43 strands almost reaching the 360 T/m required by the optics so far.

III. Prospective Steps

A. 0.7 mm strand cable layout

Based on the previous experiments, a cable made of a 0.85 mm strands is potentially too thick to be wound in a quadrupole configuration on a 50 mm diameter aperture. Therefore, a brief analysis of the performance allowed by a cable made of 0.7 mm strands was performed. Four 2D magnet cross-sections were designed each with a different number of strands in the cable: 30, 32, 36 and 40. The four designs are made of 2-layer coils where the first layer has 9 cable turns and the second one has 12 cable turns. The field quality was kept with all the harmonics below one unit. The four designs rely on the same critical current density (see section II), a hotspot temperature of 350 K with a time delay of 30 ms [3] a load-line margin of 20% at 1.9 K. To compare the designs, the following values are extracted: the gradient at nominal (Fig. 15), the peak field (Fig. 16), the nominal current value (Fig. 17), the copper/non-copper ratio of the strands (Fig. 18) and the stored energy (Fig. 19). The cross-sections are reported in Fig. 20. To provide an additional reference the four designs were re-optimized considering a loadline margin of 16% all the other constrains being equal. It is worth noticing that initially, at the beginning of the study on the FCC Main Quadrupoles, the cable layout made of 0.7 mm strands was discarded because the optics required a nominal gradient target of 360 T/m that would have led to a magnet with a cable made of 43/44 strands (see the red cross in Fig. 15). Such a cable was considered not stable enough mechanically based on the windability experience gained on the 11 T dipole magnet of the Hi-Lumi project [15][17], a dipole magnet with a 60 mm aperture and wound with a cable made of 40 strands of 0.7 mm in diameter. However, last year, scientists reported about dipole field in the 14-16 T range for the FCC-hh machine [18]. Keeping the same optics than the nominal 16 T machine, a 14 T machine would require main quadrupoles with an integrated gradient scaled down to 2268 T [19]. It could be obtained with 7.2 m long quadrupoles generating 315 T/m. This is why it now makes sense to investigate 0.7 mm strand cables for the FCC Main Quadrupoles.
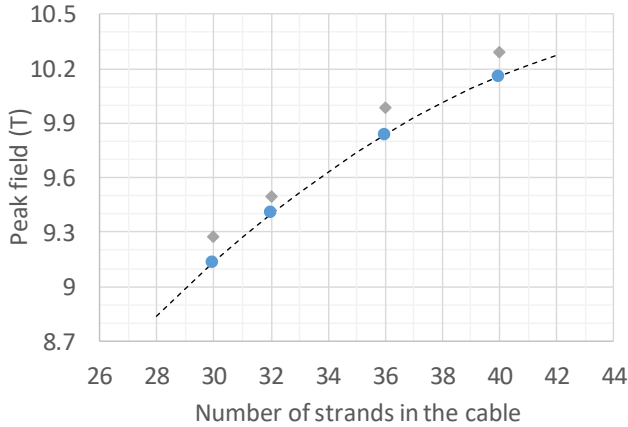

Fig. 16. Peak field of the quadrupole versus the number of strands in the cable. The blue dots represent the four 2D design data with a 20% margin which are fitted by the dash curve. The grey squares are additional data with a 16% load-line margin.

B. Magneto-thermal instabilities

A drawback of a compact 2-layer quadrupole is a high current density in the strands at a medium field range (8-12 T) potentially leading to magneto-thermal instabilities [20]. In Fig. 21, the superconductor current density in the four previous designs is reported as well as the critical current density curve. In addition the superconductor current density of a previous 4-layers quadrupole design, made of a cable with 36 strands of 0.7 mm in diameter and a copper/non-copper ratio of 2.1, is showed by a green cross (see details in [2]). Actually, 4-layer designs should finally be reconsidered for the FCC-hh Main Quadrupoles to try to overcome potential magneto-thermal instabilities by relaxing the constraint of compactness. These designs would also have the advantage of using smaller cables, potentially easier to wind. This point will require to be carefully analyzed in the future.
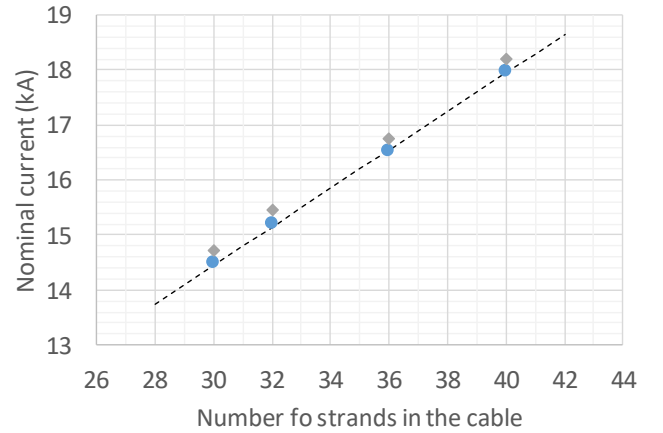

Fig. 17. Current flowing through the cable with respect to the number of strands in it. The blue dots represent the four 2D design data with a 20% margin which are fitted by the dash curve. The grey squares are additional data with a 16% loadline margin.
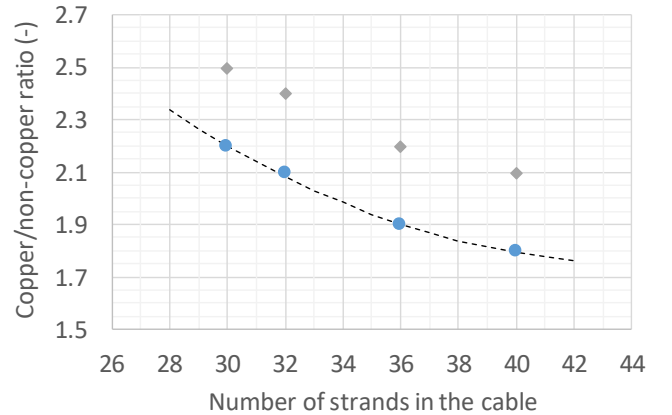

Fig. 18. The copper/non-copper ratio of the strands which is a balance between the loadline margin and the hotspot temperature with respect to the number of strands in the cable. The blue dots represent the four 2D design data with a 20% margin which are fitted by the dash curve. The grey squares are additional data with a 16% loadline margin.
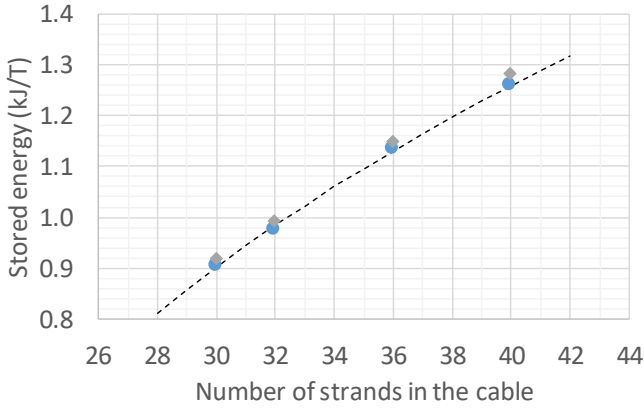
Fig. 19. Stored energy per integrated gradient in kJ/T. The value of the stored energy reported in the plot has to be multiplied by the integrated gradient in tesla to obtain the full energy of a FCC quadrupole magnet in kJ. To date, the foreseen integrated gradient is 2592 T (360 T/m, 7.2 m). The blue dots represent the four 2D design data with a 20% margin which are fitted by the dash curve. The grey squares are additional data with a 16% loadline margin.
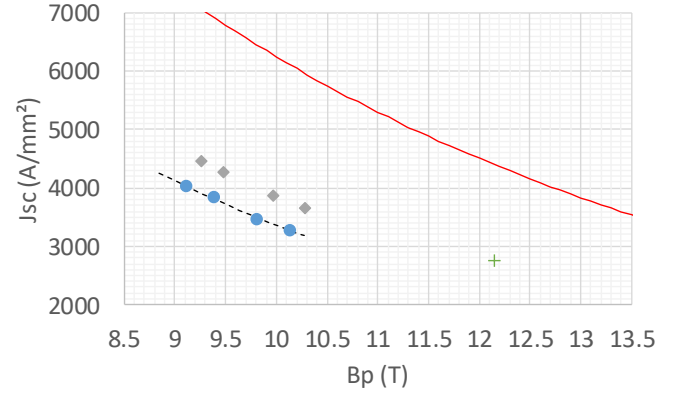

Fig. 21. Superconductor current density versus peak field. The blue dots represent the four 2D design data with a 20% margin which are fitted by the dash curve. The grey squares are additional data with a 16% loadline margin. The green cross (+) represent a previous 4 layer design based on 0.7 mm strand [2]. The red curve represent the critical current density @ 1.9 K.

IV. CONCLUSION

A 3D electromagnetic analysis of a 2-layer quadrupole was conducted in order to design its coil ends under several constraints: peak field, field quality, and windability. The design was complemented with winding trials on actual cables. The goal was to gain practical experience so as to provide useful guidance for the next design phase of the FCC-hh Main Quadrupoles, and possibly to discard some options. Several iterations of the coil ends design coupled to multiple winding trials with different tensions and a well-developed tooling were not sufficient to succeed in winding cables made of 0.85 mm strands. This paper concludes the conceptual study of the FCC-hh Main Quadrupoles carried out in the framework of a collaboration between CERN and CEA. It allows to partially clarify a concern that was raised during the first FCC week in 2015 about the "problems with curvature radius in the heads" of the quadrupole [23] with a proposal to go for small cables made of 0.7 mm strands. Nonetheless, the nominal gradient required by the optics will have to be reconsidered in light of what was demonstrated through this winding trial campaign since the achievable gradients are lower than 350 T/m. The authors questioned as well the magneto-thermal instabilities due to the high current density at medium field inherent to compact quadrupoles where load-line are very steep.
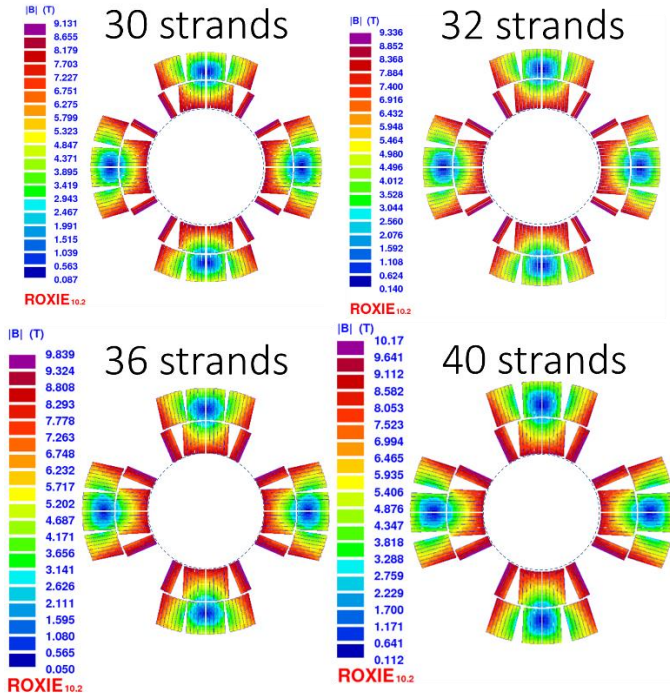

Fig. 20. Cross-section of the four quadrupoles made of different cable sizes from 30 to 40 strands of 0.7 mm in diameter. The color scale provides the field in the conductor at nominal and 20% loadline margin. The same dimension scale is used for all cross-sections.

REFERENCES

[1] The European strategy for particle physics update 2013, https://cds.cern.ch/record/1567258/files/esc-e-106.pdf

[2] C. Lorin, D. Simon, H. Felice, J-M Rifflet, D. Schoerling "Design of a Nb3Sn 400 T/m quadrupole for the Future Circular Collider", IEEE Transactions on Applied Superconductivity,4004905, 2018.

[3] C. Lorin, J. Fleiter, T. Salmi, D. Schoerling,"Exploration of a two layer Nb_3Sn designs of the Future Circular Collider Main Qaudrupoles", IEEE Transactions on Applied Superconductivity,4001005, 2019.

[4] "FCC-hh: The Hadron Collider – Future Circular Collider Conceptual Design Report Volume 3", Eur. Phys. J. Special Topics 228, 755-1107, 2019 (page 841).

[5] FCC H2020 project: http://www.eurocircol.eu/

[6] A. Chance, D. Boutin, B. Dalena, B. Holzer, D. Schulte,"Overview of arc optics of FCC-hh", 9th International Particle Accelerator Conference 2018, doi: 10.18429/JACoW-IPAC2018-MOPMF025

[7] D. Tommasini et al., "The 16 T dipole development program for FCC", IEEE TAS, vol. 27, 4000405, 2017

[8] D. Tommasini et al. "Status of the 16 T dipole development program for a Future Hadron Collider", IEEE TAS, vol. 28, 4001305, 2018

[9] C. Pes, C. Genot, C. Lorin, E. Rochepault "Preliminary 3D mechanical design of a two-layer 360 T/m FCC-hh Main Quadrrupole", to be submitted to IEEE TAS.

[10] A. Ballarino, S. Hopkins et al. "The CERN FCC conductor development program : A worldwide effort for the future generation of high-field magnets" IEEE TAS, vol. 29, 6000709, 2019

[11] S. Izquierdo-Bernudez et al. «Second-generation coil design of the Nb_3Sn low-β quadrupole for the high luminosity LHC », IEEE TAS, vol.26, 4001105, 2016

[12] B. Auchmann and S. Rüssenschuck, "Coil end design for superconducting magnets applying differential geometry methods", IEEE Transactions on Magnetics, vol.40, pp1208-1211

[13] D. Pulikowski et al., "Windability tests of Nb_3Sn Rutherford cables for HL-LHC and FCC", IEEE Transactions on Applied Superconductivity, 4003905, 2018.

[14] D. Pulikowski et al., "Testing mechanical behavior of the Nb3Sn Rutherford cable during coil winding", IEEE Transactions on Applied Superconductivity, 4802105, 2017.

[15] F. Savary et al., "Design and construction of the full-length prototype of the 11 T dipole magnet for the High Luminosity LHC project at CERN", IEEE Transactions on Applied Superconductivity, 4007106, 2018.

[16] G. Ambrosio, "Nb_3Sn high field magnets for the High Luminosity LHC upgrade project", IEEE Transactions on Applied Superconductivity, 4002107, (2015).

[17] J. Fleiter et al., "Optimization of Nb_3Sn Rutherford cables geometry for the high-luminosity LHC", IEEE Transactions on Applied Superconductivity, 4004305, (2017).

[18] "Physics Briefing Book: Input for the European Strategy for Particle Physics Update 2020", arXiv:1910.11775, CERN-ESU-004, page 173, (2019)

[19] Private discussion, A. Chance and B. Dalena, (27 sep. 2019)

[20] V.V. Kashikhin and A. Zlobin, "Magnetic Instabilities in Nb3Sn Strands and Cables", IEEE Transactions on Applied Superconductivity, 15, 2, (2005)

[21] M.D. Sumption and E. W. Collings, "Modeling current-field instabilities in High Performance Nb_3Sn Strands in Moderate Field", IEEE Transactions on Applied Superconductivity, 17, 2, (2007)

[22] B. Bordini et al., "Impact of the Residual Resistivity Ratio on the Stability of the Nb3Sn Magnets", IEEE Transactions on Applied Superconductivity, 22, 3, (2012)

[23] E. Todesco, "Magnet session summary", oral presentation, 1st FCC week, Washington 23-27 March 2015.